

Oxygen and iron in interstellar dust: An X-ray investigation

I. Psaradaki^{1,2}, E. Costantini^{1,3}, D. Rogantini^{8,1}, M. Mehdipour⁹, L. Corrales², S.T. Zeegers⁷, F. de Groot⁴, J.W.A. den Herder^{1,3}, H. Mutschke⁵, S. Trasobares⁶, C. P. de Vries¹, and L.B.F.M. Waters^{1,10}

¹ SRON Netherlands Institute for Space Research, Niels Bohrweg 4, 2333 CA Leiden, the Netherlands

² University of Michigan, Dept. of Astronomy, 1085 S University Ave, Ann Arbor, MI 48109, USA

³ Anton Pannekoek Astronomical Institute, University of Amsterdam, P.O. Box 94249, 1090 GE Amsterdam, the Netherlands

⁴ Debye Institute for Nanomaterials Science, Utrecht University, Universiteitsweg 99, 3584 CG Utrecht, Netherlands

⁵ Astrophysikalisches Institut und Universitäts-Sternwarte (AIU), Schillergäßchen 2-3, 07745 Jena, Germany

⁶ Departamento de Ciencia de los Materiales e Ingeniería Metalúrgica y Química Inorgánica, Facultad de Ciencias, Universidad de Cádiz, Campus Rfo San Pedro, Puerto Real, 11510, Cádiz, Spain

⁷ Academia Sinica, Institute of Astronomy and Astrophysics, 11F Astronomy-Mathematics Building, NTU/AS campus, No. 1, Section 4, Roosevelt Rd., Taipei 10617, Taiwan

⁸ MIT Kavli Institute for Astrophysics and Space Research, Cambridge, MA 02139, USA

⁹ Space Telescope Science Institute, 3700 San Martin Dr, Baltimore, MD 21218, USA

¹⁰ Department of Astrophysics/IMAPP, Radboud University P.O. Box 9010, 6500 GL Nijmegen, the Netherlands

November 18, 2022

ABSTRACT

Understanding the chemistry of the interstellar medium (ISM) is fundamental for the comprehension of Galactic and stellar evolution. X-rays provide an excellent way to study the dust chemical composition and crystallinity along different sight lines in the Galaxy. In this work, we study the dust grain chemistry in the diffuse regions of the ISM in the soft X-ray band (<1 keV). We use newly calculated X-ray dust extinction cross sections obtained from laboratory data in order to investigate the oxygen K and iron L shell absorption. We explore the XMM-Newton and Chandra spectra of five low-mass X-ray binaries (LMXBs) located in the Galactic plane and model the gas and dust features of oxygen and iron simultaneously. The dust samples used for this study include silicates with different Mg:Fe ratios, sulfides, iron oxides, and metallic iron. Most dust samples are in both amorphous and crystalline lattice configuration. We computed the extinction cross sections using Mie scattering approximation and assuming a power-law dust size distribution. We find that the Mg-rich amorphous pyroxene ($\text{Mg}_{0.75}\text{Fe}_{0.25}\text{SiO}_3$) represents the largest fraction of dust towards most of the X-ray sources, namely about 70% on average. Additionally, we find that $\sim 15\%$ of the dust column density in our lines of sight is in metallic Fe. We do not find strong evidence for ferromagnetic compounds, such as Fe_3O_4 or iron sulfides (FeS , FeS_2). Our study confirms that iron is heavily depleted from the gas phase into solids; more than 90% of iron is in dust. The depletion of neutral oxygen is mild, namely of between 10% and 20% depending on the line of sight.

Key words. astrochemistry, ISM:dust, X-rays:ISM

1. Introduction

Interstellar dust is ubiquitous and plays an important role in our Galaxy. Dust appears at every stage of stellar evolution, from evolved stars and supernovae (SNe) to proto-planetary discs. As the primary repository of metals in the interstellar medium (ISM), dust can regulate its thermal structure and provide the surface for chemical reactions (Henning 2010). The properties of dust grains in different regions of the ISM can provide insight into their production and destruction mechanisms and reveal the evolution history of our Galaxy.

Dust grains are characterised by their chemical composition, morphology, and size. Abundant elements such as carbon, oxygen, silicon, iron, and magnesium are the main constituents of cosmic dust. Elements such as titanium, calcium, and aluminium can be found in smaller quantities and are highly depleted from the gas phase (Jenkins 2009). Cosmic dust can roughly be divided into carbonaceous and silicate grains. Additionally, dust can consist of oxides (e.g. Fe_2O_3), sulfides (e.g. FeS), carbides, and iron inclusions, such as metallic iron (Draine 2011).

The structural properties of dust grains vary depending on the configuration of the atoms in the grain. Crystalline materi-

als are characterised by a periodic long-range order of atoms, while amorphous dust grains do not show periodic structures and present a disordered 3D network of atoms. Crystalline dust is unlikely to survive the harsh environment of the ISM. Studies of the $10\ \mu\text{m}$ silicate feature in the mid-infrared (MIR) band showed that interstellar silicate dust is mostly in amorphous form, and in particular olivines and Mg-rich pyroxenes (Kemper et al. 2004, Min et al. 2007). Moreover, X-ray absorption studies in the Si K and Mg K spectral regions recently revealed that amorphous olivine is a dominant chemical composition in the dense parts of the diffuse ISM (Zeegers et al. 2017, 2019, Rogantini et al. 2019, 2020). However, the exact ratio of olivines to pyroxenes in dust and the Mg:Fe ratio in silicates are not yet fully constrained. Resolving this issue is important because Mg-rich silicates (rather than Fe-rich) could provide an explanation for the high amount of Mg found in cometary and circumstellar grains (Min et al. 2007). At the same time, this constrains the exact amount of iron in silicates, which is still unknown.

Historically, interstellar dust has been studied in the IR and millimeter wavelengths. However, the launch of the XMM-Newton and Chandra X-ray satellites and their high-

resolution spectrometers opened up a new window for the study of the ISM and dust mineralogy. The photoabsorption edges of some of the most abundant elements in the Galaxy, such as oxygen and iron are present in the X-ray spectra of many of the brightest Galactic sources (Schattenburg & Canizares 1986, Paerels et al. 2001, Ueda et al. 2005). Today, bright X-ray binaries are used as background lights for studying the spectral features of atomic and solid species of the ISM. In particular, with high-resolution X-ray spectra we are able to distinguish the gas and solid phase abundances of individual elements and to investigate the chemical composition of dust in the ISM (e.g. Wilms et al. 2000, Costantini et al. 2012, Pinto et al. 2013 and references therein).

Oscillatory modulations, known as X-ray absorption fine structures (XAFS), are observed near the photoelectric absorption edges, and provide unique fingerprints of dust. These modulations happen when an X-ray photon gets absorbed by an atom in the dust grain, and the ejected photo-electron interacts with the neighbouring atoms. This interaction modulates the wavefunction of the photo-electron due to constructive and destructive interference between the outgoing and backscattered electron waves. The shape of the spectral modulations is determined by the local-scale atomic structure of the grain, which imprints its chemical composition and structure (see also Newville 2004, for a detailed explanation). Therefore, modelling the XAFS enables the study of the chemical composition and crystallinity of the dust.

Up-to-date models of XAFS based on laboratory experiments were recently released in the *amol* model of the SPEX X-ray fitting package¹. In particular, the iron K edge was studied by Rogantini et al. (2018) using synchrotron radiation. Synchrotron measurements were also performed in order to characterise the K edges of silicon (Zeegers et al. 2017, 2019) and magnesium (Rogantini et al. 2019). For the soft X-ray band, the oxygen K edge (Psaradaki et al. 2020, henceforth, Paper I) and the iron L edges (Costantini et al. in prep.) were studied using laboratory measurement from an electron-energy-loss spectrometer (Egerton 2011). Additionally, studies of the Fe L edges were performed by Lee et al. (2009) and Westphal et al. (2019) and for the Fe K edge by Lee & Ravel (2005). Elements such as carbon, calcium, and sulfur were studied in a similar way by Costantini et al. (2019).

In this work, we focus on the iron and oxygen content of interstellar dust. The precise whereabouts of the interstellar iron is a long-standing conundrum. Iron is known to be predominantly depleted from the gas phase into solids, with the depletion value changing slightly depending on the environment. Despite this high depletion rate of Fe, the exact composition of the Fe-bearing grains is still unclear. Iron is primarily formed in type Ia SNe and core collapse SNe. It is believed that more than 65% of the iron is injected into the ISM in the gaseous form and therefore most of its grain growth is expected to take place in the ISM (Dwek 2016).

Schalen (1965) and Kemper et al. (2002) suggested that some of the depleted cosmic iron could be in the form of pure metallic iron. Poteet et al. (2015) studied the line of sight towards ζ Ophiuchi using IR observations, and found that nearly all the Mg and Si atoms reside in amorphous silicate grains, while a substantial amount of iron resides in other compounds. Hydrodynamic simulations of Zhukovska et al. (2018) suggest that a large fraction

of iron (70%) is locked as inclusions in silicate grains, where it is protected from sputtering by SN shocks. The remaining depleted iron could reside in a population of metallic iron nanoparticles with sizes in the range of 1–10 nm. Other forms of solid-phase iron include metallic inclusions in glass with embedded metal and sulphides of interstellar origin (e.g. Keller & Messenger 2013).

Oxygen is one of the most abundant elements in the Galaxy. However, the total oxygen budget in the ISM is largely uncertain (Jenkins 2009). While oxygen is expected to be mildly depleted into dust, a significant fraction of it is missing from the gas phase at a level that cannot yet be fully explained. The combined contributions of CO, ices, and silicate and oxide dust cannot fully account for the missing oxygen in the dense regions of the ISM, and in particular at the interface between diffuse and dense ISM (Whittet 2010, Poteet et al. 2015). A possible solution to the oxygen budget problem of the ISM was proposed by Jones & Ysard (2019), who conclude that a significant fraction of oxygen in the dense ISM could exist in organic carbonate solids ($(\text{C-O}) = \text{O}$). This material maximises the O/C atom ratio (3:1) so that oxygen can be efficiently depleted without over-depleting carbon, the most likely element-depleting partner of oxygen. In this paper, we study the O K and Fe L edges simultaneously using the most up-to-date dust laboratory measurements. This is the first time that these two elements are studied together with a new accurate dust extinction model that also considers the effect of dust scattering (see paper I). We studied the iron and oxygen abundances and depletions² in five sight lines along the Galactic plane, with column densities of $< 5 \times 10^{21} \text{ cm}^{-2}$. This paper is organised as follows. In Section 2, we present the sample of X-ray binaries and in Section 3 we show the X-ray data used for this work. The methodology used for the spectral fitting of the ISM is explained in Section 4. Finally, in Section 5 we discuss our results, and give our conclusions in Section 6.

2. X-ray sources

To study the O K and Fe L edges simultaneously, we adopt five low-mass X-ray binaries (LMXBs) as background sources that are suitable to model the ISM absorption. LMXBs are excellent candidates due to their high flux and the absence of emission features that could complicate the analysis. The depth and visibility of the X-ray photoabsorption edges is highly dependent on the ISM column density in the foreground of an X-ray binary. We therefore select sources with a column density in the range of $1 - 5 \times 10^{21} \text{ cm}^{-2}$ in order to guarantee a large optical depth for both the O K and Fe L edges. The flux limit has been chosen to be larger than $1 \times 10^{-9} \text{ erg}^{-1} \text{ s}^{-1} \text{ cm}^{-2}$ in the 0.1-2 keV band to ensure a high signal-to-noise-ratio(S/N) spectrum.

Another requirement is the availability of data from both XMM-Newton and Chandra public archives. The selected sample of sources as well as the obs. ID and exposure times are listed in Tables 1 and 2. Table 1 also shows the distance to the source, the column density (N_{H}) taken from the HI4PI Collaboration et al. (2016), the reddening values $E(B-V)$ when available, and the calculated column density ($N_{\text{H}}^{E(B-V)}$) derived using the conversion $N_{\text{H}}/E(B-V) = 5.8 \times 10^{21} \text{ H cm}^{-2} \text{ mag}^{-1}$ (Draine 2011). Figure 1 presents the projection of the X-ray sources on the Galactic plane, while Fig. 2 shows the sources on an all-sky

¹ <https://spex-xray.github.io/spex-help/models/amol.html>

² In this work, we define depletion of an element using the ratio of the dust abundance to the total abundance of a given element (both gas and dust).

map of the Galactic dust emission at a wavelength of $100\ \mu\text{m}$ (Schlegel et al. 1998).

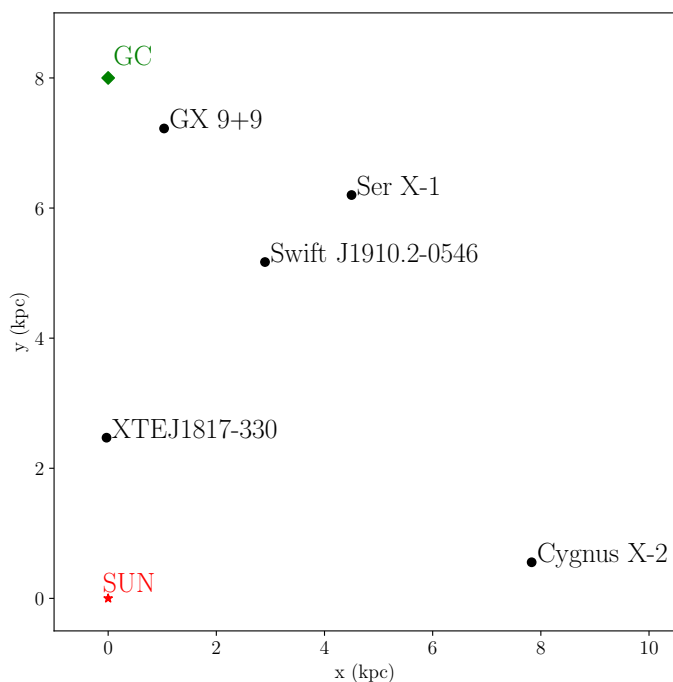


Fig. 1. Projection of the X-ray sources on the Galactic plane. The distance between the sun and the Galactic centre is assumed to be 8 kpc.

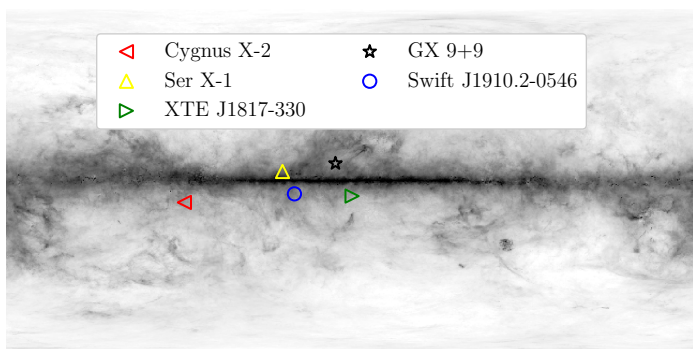


Fig. 2. X-ray sources plotted on a $100\ \mu\text{m}$ full-sky map, adopted from Schlegel et al. (1998).

3. Data processing and reduction

In order to best study the narrow absorption features of gas and dust present in the soft X-ray band ($< 1\ \text{keV}$), we combine the capabilities of the currently available high-resolution X-ray spectrometers on board XMM-Newton and Chandra satellites. To study the oxygen K-edge region, we use the Reflection Grating Spectrometers (RGS, den Herder et al. 2001) of XMM-Newton, which has a resolving power of $R = \frac{\lambda}{\Delta\lambda} \gtrsim 400$ and an effective area of approximately $45\ \text{cm}^2$ in this spectral region.

Chandra carries a high-spectral-resolution instrument called the High Energy Transmission Grating (HETGS, Canizares et al. 2005), which consists of two sets of gratings, the medium-energy grating (MEG) and the high-energy grating (HEG). For the iron L-edges, we use Chandra data because of the higher spectral resolution of HETGS/MEG around the Fe L-edges. The MEG has

an effective area of approximately $7\ \text{cm}^2$ and a resolving power of $R = \frac{\lambda}{\Delta\lambda} \gtrsim 760$ around the iron L-edges, which makes it the most suitable instrument to study the XAFS with archival data in this spectral region. A similar approach, using combined information from XMM-Newton and Chandra data, was presented in Costantini et al. (2012). All the observation IDs (obsid) used in this paper are listed in Tables 1 and 2.

3.1. XMM-Newton

We obtain the RGS data from the XMM-Newton public archive³. We reduced the data using the Science Analysis Software, SAS (ver.18). We first ran the *rgsproc* command to create the event lists, and then we filtered the RGS event lists for flaring particle background using the default value of 0.2 counts/sec threshold. The bad pixels are excluded using *keepcool=no* in the SAS task *rgsproc*. In bright sources, some areas of the grating data may be affected by pile-up, which can change the shape of the spectrum below $19\ \text{\AA}$. To avoid the effect of pile-up, we ignore the region of the spectra shorter than $19\ \text{\AA}$. In this analysis, we are cautious when combining different observations of the same source in order to avoid artifacts in the spectrum created from the merger. However, when the spectral shape and flux of certain observations does not vary, or the data have been acquired in the same epoch and can be superimposed, we combine them using the SAS command *rgscombine*. This allows us to obtain a single spectrum with higher S/N.

3.2. Chandra

The Chandra observations used in this work were downloaded from the Transmission Grating Catalogue⁴ (TGCat, Huenemörder et al. 2011). For each observation, we combine the positive and negative spectral orders using the X-ray data analysis software, CIAO (version 4.11, Fruscione et al. 2006). Depending on the availability of the data, we use observations taken in either timing (TE) mode or continuous clocking (CC) mode. To avoid pile-up when working with bright sources, we ignore the region of the spectra below $10\ \text{\AA}$. Similarly, with the XMM-Newton observations, if the spectral shape of a certain source is steady, and the spectra do not present any variations, we combine the different observations using the CIAO tool *combine_grating_spectra*.

4. Spectral fitting of the ISM

4.1. The two-edge fit

In this work, we fit the O K- and Fe L-edges simultaneously. For our modelling, we use the software SPEctral X-ray and UV modelling and analysis, SPEX, version 3.06.01⁵ (Kaastra et al. 1996; Kaastra et al. 2018). We fit the Chandra data in the range of $10\text{--}19\ \text{\AA}$ and the XMM-Newton spectrum between 19 and $35\ \text{\AA}$. This wavelength range covers an area that is sufficiently broad around the edges and excludes areas that can complicate our fit and hamper the XAFS modelling.

The XMM-Newton and Chandra data of each source were obtained at different epochs and therefore the continuum shape might be different due to variability intrinsic to the source. To take this variability into account, we use the *sectors* option

³ <http://nxsas.esac.esa.int/nxsas-web/>

⁴ <http://tgcath.mit.edu/tgSearch.php?t=N>

⁵ <http://doi.org/10.5281/zenodo.2419563>

Table 1. XMM–Newton RGS observation log

Source	obs. ID	exposure time (ks)	distance (kpc)	Galactic coordinates (l,b)	N_{H}	$E(B-V)$	$N_{\text{H}}^{E(B-V)}$
Cygnus X–2	0303280101	32	8-11 ^(a)	(87.3,-11.3)	1.9	0.4 ± 0.07 ⁽¹⁾	2.3 ± 0.4
	0561180501	24					
	0694860301	36					
GX 9+9	0090340101	11	5-7 ^(b)	(8.5,9)	1.9	0.1-0.4 ⁽²⁾	0.6-2.3
	0090340601	22					
	0084020401	22					
Ser X–1	0084020501	22	7.7 ± 0.9 ^(c)	(36.1,4.8)	4.4	0.4-1.5 ⁽³⁾	2.3-8.7
	0084020601	22					
	0084020601	22					
SWIFT J1910.2–0546	0691271401	28	6 ^(d)	(29.9,-6.8)	2.24	-	-
XTE J1817–330	0311590501	20	1-4 ^(e)	(359.8,-8)	1.5	0.1-0.5 ⁽⁴⁾	0.6-3

Notes. The symbol N_{H} represents the hydrogen column density in 10^{21} cm^{-2} from HI4PI Collaboration et al. (2016), and $N_{\text{H}}^{E(B-V)}$ is the column density in 10^{21} cm^{-2} estimated from the reddening values $E(B-V)$ taken from: ⁽¹⁾McClintock et al. (1984), ⁽²⁾Shahbaz et al. (1996), ⁽³⁾Thorstensen et al. (1980), ⁽⁴⁾Torres et al. (2006). Distances are from: ^(a)Cowley et al. 1979 & Smale 1998, ^(b)Christian & Swank (1997) & Vilhu et al. (2007), ^(c)Galloway et al. (2008), ^(d)Reis et al. (2013), ^(e)Sala & Greiner (2006). To convert from $E(B-V)$ to N_{H} we used the conversion $N_{\text{H}}/E(B-V) = 5.8 \times 10^{21} \text{ H cm}^{-2} \text{ mag}^{-1}$ (Draine 2011).

Table 2. Chandra observation log

Source	obs. ID	instrument/mode	exposure time (ks)
Cygnus X–2	8170	HETGS/CC	65
	8599	HETGS/CC	60
GX 9+9	11072	HETGS/TE	95
	703	HETGS/TE	20
Ser X–1	700	HETGS/TE	77
SWIFT J1910.2–0546	14634	HETGS/CC	30
XTE J1817–330	6617	HETGS/CC	47

in SPEX. With this option, each dataset is allocated to a specific sector. In this way, the continuum parameters (which are variable over time) for each dataset are treated independently and allowed to vary freely while the ISM model is jointly fitted to all the data. Because we use a narrow energy band for each observation, we do not need to fit the broadband continuum with any physical models. Hence, we use a phenomenological power-law model (`pow` in SPEX) and a black body component (`bb`) to describe the continuum in this energy range.

We apply a binning on our data of a factor of 2, which improves the S/N while the data are still oversampling the spectral resolution of the instrument and we are not losing accuracy. We further adopt C -statistics (C_{stat}) to evaluate the goodness of our fit (Cash 1979, Kaastra 2017). All uncertainties are provided at 1σ significance. Also, in our analysis, we use proto-Solar abundance units from Lodders & Palme (2009). A step-by-step description of our spectral fitting procedure is presented in Section 4.2.

4.2. Fitting procedure

The fitting procedure described in this section is applied to all the sources presented in Figure 1.

The multi-phase gas modelling

To characterise the neutral Galactic absorption, we adopt the hot model of SPEX (de Plaa et al. 2004). For a given temperature and set of abundances, this model calculates the ionisation balance and then determines all the ionic column densities by scaling to the prescribed total hydrogen column density. At low temperatures ($\sim 0.001 \text{ eV} \sim 10 \text{ Kelvin}$), the hot model mimics the neutral gas. The free parameters here are the hydrogen column density (N_{H}) and the temperature (kT , where k is the boltzmann constant) as well as the relative abundance of oxygen, iron, silicon, and magnesium.

Two additional hot models are used to take into account the weakly and mildly ionised gas. In this way, we probe the different ISM phases along the line of sight of each source. The column densities and temperatures of the hot components derived from our spectral fitting are listed in Table 3.

We further take into account the absorption from a hot gas (e.g. O VII, O VIII) using the slab model in SPEX. This model calculates absorption by a slab of optically thin gas, where the column densities of the ions are fitted individually and are independent of each other. The nature of these absorption lines is still debated; they have been attributed to either warm absorbers intrinsic to the binary system or to a hot phase of the ISM. Investigation of the origin of these lines is outside the scope of this paper, and therefore we do not provide a physical interpretation for them.

Table 3. Best-fit parameters of the ISM gas-phase components.

Source		hot # 1	hot # 2	hot # 3
Cygnus X-2	N_{H}	1.7 ± 0.3	0.04 ± 0.01	0.027 ± 0.007
	kT	$0.001 (f)$	2.6 ± 0.6	14.7 ± 0.1
GX 9+9	N_{H}	2.1 ± 0.1	0.10 ± 0.02	0.027 ± 0.005
	kT	$0.001 (f)$	2.6 ± 0.8	210 ± 23
Ser X-1	N_{H}	5.5 ± 0.1	0.4 ± 0.1	0.11 ± 0.05
	kT	$0.001 (f)$	2.2 ± 0.8	14 ± 2
SWIFT J1910.2-0546	N_{H}	3.20 ± 0.04	0.03 ± 0.01	0.022 ± 0.005
	kT	$0.001 (f)$	13 ± 1	145 ± 10
XTE J1817-330	N_{H}	1.50 ± 0.01	0.09 ± 0.02	0.03 ± 0.01
	kT	$0.001 (f)$	3.0 ± 0.7	10 ± 2

Notes. Best-fit parameters of the three hot components. The symbol N_{H} represents the hydrogen column density in 10^{21} cm^{-2} and kT represents the temperature in eV. The temperature of the neutral gas component (hot # 1) is frozen to the minimum value in order to produce neutral species only. This is noted with the symbol f .

The dust modelling

In addition to the gas components, we model the dust absorption in the O K and Fe L edges with a custom version of the `amol` model in SPEX. This model calculates the transmission of a dust component, and the free parameter is the dust column density. We use the recently implemented dust extinction cross sections for the oxygen K-edge presented in Paper I. For the iron L-edges, we use new dust extinction cross sections computed using the same laboratory measurements and methodology (Costantini et al. in prep). The laboratory experiment and post-processing are explained in detail in Paper I (also see Zeegers et al. 2017; Rogantini et al. 2018). In summary, we calculated the total extinction for oxygen using Mie theory (Mie 1908), and in particular the Python library `miepython`⁶. For the iron models, we calculated the total extinction cross section using anomalous diffraction theory (ADT, van de Hulst 1957). For both oxygen and iron, a Mathis-Rumpl-Nordsieck dust size distribution is assumed (MRN, Mathis et al. 1977), which follows a power-law distribution, $dn/da \propto a^{-3.5}$, where a is the grain size with a minimum cut-off of $0.005 \mu\text{m}$, and a maximum of $0.25 \mu\text{m}$.

The minerals. In Table 4, we summarise the different types of dust mineralogy used in this work by specifying their chemical formula and lattice structure (i.e. crystallinity). Our dust samples include silicates, such as olivines and pyroxenes, with varying Mg:Fe ratio. We also include oxides, iron sulfides, and metallic iron. The latter has been adopted from the literature (Kortright & Kim 2000, Lee 2010) and has been shifted according to the energy calibration value supplied by Fink et al. (1985). For all the compounds, the scattering component of extinction has also been included here using the MRN dust size distribution as mentioned above.

Fitting method. The `amol` model can fit up to four different dust compounds simultaneously in a given fitting run. We test all the possible combinations of four dust species among the 13 samples assuming that the interstellar dust mixture can be described with four components at most. The number of different combinations is given by the equation:

Table 4. List of dust samples.

#	Compound	Chemical Formula	Form
1	Olivine	MgFeSiO_4	amorphous
2	Olivine	$\text{Mg}_{1.56}\text{Fe}_{0.4}\text{Si}_{0.91}\text{O}_4$	crystalline
3	Pyroxene	$\text{Mg}_{0.6}\text{Fe}_{0.4}\text{SiO}_3$	amorphous
4	Pyroxene	$\text{Mg}_{0.6}\text{Fe}_{0.4}\text{SiO}_3$	crystalline
5	Enstatite	MgSiO_3	crystalline
6	Enstatite	MgSiO_3	amorphous
7	Fayalite	Fe_2SiO_4	crystalline
8	Forsterite	Mg_2SiO_4	crystalline
9	Pyroxene	$\text{Mg}_{0.75}\text{Fe}_{0.25}\text{SiO}_3$	amorphous
10	Magnetite	Fe_3O_4	crystalline
11	Troilite	FeS	crystalline
12	Pyrit Peru	FeS_2	crystalline
13	Metallic iron	Fe	-

Notes. The samples 2, 5, and 11 are natural and 8, 10, and 12 are commercial products. Samples 1, 3, 4, 6, 7, and 9 are instead synthesised in the laboratories at the Astrophysikalisches Institut, Universitäts-Stenwarte (AIU), and Osaka University. We adopted the metallic iron presented by Kortright & Kim (2000) and Lee (2010), with a shift in energy according to the work of Fink et al. (1985).

$$C_{e,c} = \frac{e!}{c!(e-c)!} \quad (1)$$

where e is the number of the available edge profiles and c the combination class. This gives us 715 dust mixtures to choose from when fitting the spectra for each source.

In Figure 4.2 we present, for all the sources, the best fit in the O K- and Fe L-edges. In Table 5 we list the best-fit dust mixtures with the column densities of each dust compound contributing to the absorption. The same table also provides the calculated dust-to-gas mass ratio (D) for every line of sight. We calculated the dust mass while accounting for the mass of the elements that make up the best-fit minerals, and we assume that the gas mass is dominated by hydrogen and helium. Figure 4.2 presents the best fit for a selected source in detail, namely SWIFT J1910.2-0546. The bottom panel shows the transmission of gas and dust components used in the fit. The Fe L-edge shape is dominated by the dust absorption, while the

⁶ <https://miepython.readthedocs.io/en/latest/>

fit to the O K edge is dominated by gas features. However, the dust absorption in the O K edge is not negligible, but covers a broad region around the edge and improves the fit around 23.3 Å, where the scattering component of extinction is present (see Paper I).

Model selection. Following the methodology used in Paper I and in Rogantini et al. (2020), we evaluate the best fit among the various dust mixtures using the *Akaike information criterion* (AIC, Akaike 1974). AIC provides a robust and fast way to select the models that are statistically similar to the best fit. Traditional likelihood-based methods for model selection provide a mechanism for estimating the unknown parameters of a model as these latter have a specified dimension and structure. Akaike (1974) extends this paradigm by considering a framework in which the model dimension is also unknown (Feigelson & Babu 2012). AIC treats all the models symmetrically, not requiring an assumption that one of the candidate models is the correct model. It can therefore be used for both nested and non-nested models. In our case, the models are non-nested and have the same number of free parameters. In practice, this method allows a quick comparison of the candidate models by comparing the C-statistic value of every fit with the best one. The AIC value is given by:

$$\text{AIC} = 2k - 2\ln(\mathcal{L}_{\max}) \quad (2)$$

where k is the number of fitted parameters of the model and \mathcal{L}_{\max} is the maximum likelihood value. The C-statistics value and the maximum likelihood are related as $\text{Cstat} = -2\ln(\mathcal{L})$ (Cash 1979). We are not directly interested in the AIC value; we calculate the AIC difference (ΔAIC) over all candidate models with respect to the model that has the lowest AIC value. Models with $\Delta\text{AIC} < 4$ are considered comparable and can fit the spectrum equally well, while models with $\Delta\text{AIC} > 10$ can be ruled out (Burnham & Anderson 2002).

Figure 4.2 presents the relative fraction of each dust compound using the AIC criteria. In particular, the bar chart shows the results for the models with $\Delta\text{AIC} < 4$ including all the fits with similar significance compared to the best fit (about 50 on average).

5. Discussion

5.1. Silicate mineralogy

Our analysis of the five X-ray binaries shows that Mg-rich amorphous pyroxene ($\text{Mg}_{0.75}\text{Fe}_{0.25}\text{SiO}_3$) is the dominant compound in most sight lines. Figure 4.2 presents the relative fraction of column density contributed by each sight line to the dust content chemical compound towards the five sources. For this plot, we consider models with $\Delta\text{AIC} < 4$. In particular, we find that Mg-rich amorphous pyroxene accounts for approximately 70% of the dust column towards Cygnus X-2, Swift J1910.2-0546, XTE J1817-330, and Ser X-1.

The results on the silicate mixture of dust are broadly consistent with previous studies at the IR wavelengths. Min et al. (2007) studied the spectral shape of the 10 μm interstellar extinction feature towards the Galactic centre. These authors found that interstellar silicates are magnesium rich and that the stoichiometry lies between pyroxene and olivine types. The authors suggest that the high magnesium content of amorphous silicates provides an explanation for the relatively high amount of magnesium found in cometary and circumstellar grains. Other IR

studies have also shown that the silicate feature can be modelled with a mixture of Mg-rich olivines and pyroxenes (Molster et al. 2002, Chiar & Tielens 2006).

In our study, we find a different dominant silicate mineralogy from those previously discovered by Zeegers et al. (2019, henceforth Z19) and Rogantini et al. (2020, henceforth R20) using the same dust laboratory samples. Our analysis shows that amorphous pyroxene ($\text{Mg}_{0.75}\text{Fe}_{0.25}\text{SiO}_3$) is the dominant dust compound. Z19 and R20 studied the gas and dust absorption on the silicon and magnesium K edges showing that amorphous olivine (MgFeSiO_4) represents most of the dust in the dense environments of the ISM ($\sim 10^{22} \text{ cm}^{-2}$). Here, we probe more diffuse regions of the ISM ($\sim 10^{21} \text{ cm}^{-2}$) and different lines of sight and therefore variations in the results are possible.

Moreover, Demyk et al. (2001) performed irradiation experiments exposing crystalline olivine and pyroxene materials to high-energy ions. These authors found that under He^+ irradiation, the olivine loses Mg and O and therefore the silicate composition could evolve from olivine to pyroxene in the diffuse ISM. Our lines of sight probe regions with typical gas densities that are an order of magnitude lower than those of R20 and Z19. It is possible that the degree of processing of silicates along these different sight lines differs. Our sight lines could represent a population of dust that is losing oxygen and magnesium atoms to the gas phase, which could lead to a more pyroxene-like stoichiometry. In other, higher density environments this process may be less efficient, or accretion of atoms to dust grains may become important.

GX 9+9 is an outlier. Amorphous olivine (MgFeSiO_4) is the dominant compound in this line of sight, contrary to amorphous Mg-rich pyroxene ($\text{Mg}_{0.75}\text{Fe}_{0.25}\text{SiO}_3$) found towards the other X-ray sources. It is possible that with GX 9+9 we are probing a different ISM environment. We examined the 3D maps of interstellar dust reddening based on Pan-STARRS 1 and 2MASS photometry and Gaia parallaxes⁷ (Green et al. 2019 and references therein). These maps trace the dust reddening both as a function of angular position on the sky and distance. Using these maps, we find that there is a steep jump in the line-of-sight reddening towards GX 9+9. This suggests that there is a dense cloud of dust in front of GX 9+9. The profiles of reddening versus distance for the other targets in this study do not generally exhibit steep jumps. Instead, the amount of reddening increases more gradually with distance, suggesting that the dust along these sight lines is more diffuse in its distribution. We therefore conclude that the GX 9+9 sight line is different from the others, possibly containing a denser cool cloud, which might explain why amorphous olivine fits this spectrum better.

We find an upper limit on the silicate crystallinity of 15%. Our results are consistent with those of R20 and Z19. The authors found that 0% – 30% of dust is in crystalline configuration, depending on the line of sight. Additionally, the shapes of the 9.7 μm and 18 μm features in the IR suggest that the upper limit of crystallinity is constrained to 2.2% (Kemper et al. 2004). If there is a discrepancy between the IR and the X-ray band, it could be attributed to the nature of X-rays, which are sensitive to a short range order of atoms, meaning that we may observe crystallinity in partly glassy materials. Moreover, X-rays provide a probe of larger grains, while the IR emission is dominated by the smaller dust sizes. It is therefore possible that X-rays are penetrating a portion of the grain that is shielded from cosmic rays, which destroy the crystalline structure.

⁷ <http://argonaut.skymaps.info/>

Table 5. Dust column densities for each chemical compound in 10^{16} cm^{-2} which corresponds to the best fit of each source.

Compound #	Dust compound	Cygnus X-2	GX 9+9	Ser X-1	SWIFT J1910.2-0546	XTE J1817-330
1	<i>a</i> – MgFeSiO ₄	-	4.5 ± 0.8	-	-	-
2	<i>c</i> – Mg _{1.56} Fe _{0.4} Si _{0.91} O ₄	-	<1.2	-	5.3 ± 3.4	-
3	<i>a</i> – Mg _{0.6} Fe _{0.4} SiO ₃	<1.8	-	-	-	<1
4	<i>c</i> – Mg _{0.6} Fe _{0.4} SiO ₃	-	-	-	-	<3
5	<i>c</i> – MgSiO ₃	-	-	-	-	-
6	<i>a</i> – MgSiO ₃	-	<0.4	-	-	-
7	<i>c</i> – Fe ₂ SiO ₄	-	-	-	-	-
8	<i>c</i> – Mg ₂ SiO ₄	-	-	-	-	-
9	<i>a</i> – Mg _{0.75} Fe _{0.25} SiO ₃	8 ± 1	-	17.1 ± 0.2	9 ± 4	8 ± 1
10	<i>c</i> – Fe ₃ O ₄	-	-	<0.9	-	-
11	<i>c</i> – FeS	-	-	-	-	-
12	<i>c</i> – FeS ₂	<1	-	<0.5	<0.2	-
13	Fe metal	1.8 ± 0.9	<1.3	8 ± 2	3 ± 1	2.3 ± 0.7
$C_{\text{stat}}/d.o.f.$		1311/1056	2098/1667	1005/787	2122/1837	1188/1002
D		0.005	0.004	0.003	0.004	0.007

Notes. The symbol *a* refers to amorphous compounds and *c* to crystalline. In the last rows, we present the C_{stat} of the best fit in every source compared to the degrees of freedom (*d.o.f.*) and the dust-to-gas mass ratio (D).

5.2. Abundances and depletions of O and Fe

We calculated the abundances and depletions of oxygen and iron for the different lines of sight probed in this study, and present the results in Table 6. The calculations are based on the parameters of the best-fit model. In the first column, we list the sources used in this study. In the second (N_{gas}) and third (N_{dust}) columns, we list the gas and dust column density, respectively. We note that the dust column density for O and Fe can be calculated from the values in Table 5. For example, column densities of oxygen molecules in Table 5 that include three oxygen atoms can be multiplied by three to get the total dust columns listed in Table 6. In the next two columns, we show the abundances of the neutral gas and dust with respect to hydrogen. Column 6 shows the total abundance of gas and dust with respect to proto-Solar abundances of Lodders & Palme (2009) and in column 7 we present the depletion of each element into dust, that is, the fraction of oxygen and iron that has been locked up in dust grains with respect to the total.

We find that about 10%-20% of the neutral oxygen is depleted into dust. In most lines of sight, oxygen is slightly overabundant, being about 1.2-1.4 times the Solar value. Our results are consistent with those of previous studies of the O K and Fe L spectral regions. Costantini et al. (2012) studied the gas and dust absorption towards the Galactic X-ray binary 4U1820-30, simultaneously fitting the O K and Fe L-edges with XMM-Newton and Chandra observations, respectively. These authors found that oxygen is slightly overabundant, that is, by a factor of 1.23 times the Solar value, and 20% of oxygen is depleted into dust. Pinto et al. (2013) studied the ISM composition towards nine Galactic LMXBs. These authors studied the O K and Fe L-edges simultaneously using XMM-Newton observations, and found that significant amounts of oxygen and iron are contained in solids, 15%-25% and 65%-90%, respectively.

More than 90% of iron in our study is depleted into dust grains. Within the errors, iron is found to be consistent with the Solar value, or slightly under-abundant. The under-abundance of iron might be attributed to the size distribution of the dust grains studied here. In this study, we are using an MRN dust size distribution (0.005 – 0.25 μm , Mathis et al. 1977); however, some

of the depleted iron could be included in larger grains with sizes above 0.25 μm .

Self-shielding could contribute to the reduction of the total iron column available for photoelectric absorption (Wilms et al. 2000). In this case, strong absorption prevents X-rays from penetrating the inner portions of the dust grain, and a smaller fraction of the total metal column contributes to the absorption edge (Corrales et al. 2016). Self-shielding is included in our study; we have taken into account the total extinction (scattering + absorption) cross section into our spectral modelling. However, this effect is only expected to become noticeable for regions of the ISM that contain large grains, closer to the upper limit of the dust size distribution used in this study. It is therefore possible that some of the depleted iron resides in large-grain populations, that is, greater than 0.25 μm . This will be examined in a future study.

5.3. What form does solid iron take?

Identifying the composition of solid-phase iron is important in order for us to understand how dust grows in the ISM. About 90% of the total amount of iron is missing from the gas phase and is believed to be locked up in dust grains. Some studies suggest that more than 65% of the iron is injected into the ISM in gaseous form. Therefore, most of its grain growth should take place in the ISM (Dwek 2016). In this work, we are able to identify the solid compounds that make up the 90% of depleted iron. In addition to silicates discussed in Section 5.1, we find that on average 15% of the total dust column in our sight lines is in the form of metallic iron.

Additional reservoirs of iron other than silicates and metallic iron have been extensively discussed in the literature. Ferromagnetic inclusions (Fe₃O₄) could be possible iron carriers. In particular, dust grain inclusions of ferromagnetic material, such as magnetite, have been discussed in view of grain alignment because of their ferromagnetic properties (Hoang & Lazarian 2016). Iron sulfides are other possible iron carriers. However, the amount of depleted sulfur still remains an open question. Here, we find that less than 2% of the total dust column density in our

Table 6. Oxygen and iron column densities, abundances, and depletions.

Oxygen						
Source	N_{gas} 10^{18} cm^{-2}	N_{dust} 10^{17} cm^{-2}	A_{gas} 10^{-4} H^{-1}	A_{dust} 10^{-4} H^{-1}	A/A_{\odot}	δ_X
Cygnus X-2	1.1 ± 0.1	2.5 ± 0.3	6.4 ± 0.6	1.5 ± 0.2	1.3 ± 0.1	0.18 ± 0.02
XTE J1817-330	1.06 ± 0.06	2.7 ± 0.4	7.1 ± 0.4	1.6 ± 0.3	1.4 ± 0.1	0.18 ± 0.03
Ser X-1	3.4 ± 0.1	5 ± 2	6.2 ± 0.2	1.0 ± 0.4	1.20 ± 0.07	0.13 ± 0.05
SWIFT J1910.2-0546	2.3 ± 0.1	4.8 ± 1.7	7.30 ± 0.03	1.5 ± 0.6	1.4 ± 0.1	0.17 ± 0.06
GX 9+9	1.6 ± 0.1	2.2 ± 0.4	7.9 ± 0.5	1.1 ± 0.3	1.45 ± 0.12	0.12 ± 0.02
Iron						
Source	N_{gas} 10^{18} cm^{-2}	N_{dust} 10^{17} cm^{-2}	A_{gas} 10^{-6} H^{-1}	A_{dust} 10^{-5} H^{-1}	A/A_{\odot}	δ_X
Cygnus X-2	0.004 ± 0.001	0.4 ± 0.1	2.6 ± 0.7	2.4 ± 0.5	0.79 ± 0.16	0.98 ± 0.02
XTE J1817-330	0.007 ± 0.002	0.4 ± 0.1	2 ± 1	2.9 ± 0.5	1.02 ± 0.16	0.93 ± 0.16
Ser X-1	0.003 ± 0.002	1.20 ± 0.05	0.4 ± 0.7	2 ± 1	0.8 ± 0.3	0.98 ± 0.03
SWIFT J1910.2-0546	0.010 ± 0.004	0.7 ± 0.3	3.3 ± 1.3	2.3 ± 0.1	0.8 ± 0.3	0.87 ± 0.08
GX 9+9	< 0.005	0.5 ± 0.1	< 2.5	2.5 ± 0.6	0.8 ± 0.1	> 0.98

Notes. N_{gas} and N_{dust} correspond to the total column density of gas and dust respectively for each element (O and Fe). A_{gas} and A_{dust} indicate the abundances of oxygen and iron in gas and dust (with respect to hydrogen). A/A_{\odot} is the total abundance ratio (gas+dust) in proto-Solar abundance units of [Lodders & Palme \(2009\)](#) and δ_X is the depletion of the X element from the gas phase i.e. the fraction of that element locked up in dust. The abundances and depletions were calculated using the values from the best-fit model.

lines of sight is in other forms, such as sulfides (FeS and Fe₂S) or iron oxides (magnetite, Fe₃O₄).

Our study reveals that $\sim 40\%$ of the dust-phase Fe atoms are in metallic form, and the remaining $\sim 60\%$ of iron is in the form of silicates. This result is an average from all the sources, calculating the mass density of iron atoms that reside in each chemical compound. As the amount of sulfides and other Fe-bearing compounds is significantly smaller, we do not include them in this calculation. [Tamanai et al. \(2017\)](#) discuss the distribution of Fe in presolar silicate grains originating from AGB stars and SNe. These authors find that a significant fraction of iron atoms are concentrated in metallic Fe nano-particles, and not distributed in the silicate lattice. In particular, [Tamanai et al. \(2017\)](#) show that there are a wide range of Fe atom fractions in metallic Fe, with the value going from 0.2 to 1. Our value (0.4 or 40%) is within the limits of their study. We therefore conclude that it is possible that a significant fraction of Fe that condenses in stellar environments could reside in the form of metallic iron.

[Draine & Hensley \(2021\)](#) discuss the fraction of solid-phase iron (f_{Fe}) included in metallic form. Their value of f_{Fe} is considered to be small, $< 10\%$, due to the ferromagnetic properties of metallic iron which would generate thermal magnetic-dipole emission with unusual spectral and polarisation characteristics ([Draine & Hensley 2013](#)). Our value of $\sim 40\%$ (on average) departs significantly from this concept. Table 2 of [Draine & Hensley \(2021\)](#) presents the chemistry of grains composing the ‘astrodust’ material, showing that a large amount of the solid-phase iron is in other compounds such as sulfides or magnetite. The advantage of studying the XAFS in the Fe L-edges is that we can get a direct measure of the Fe content in dust; however, we do not exclude possible biases affecting this result. Metallic iron is the only compound taken from the literature and therefore uncertainties in the energy calibration of the model might be possible.

5.4. The oxygen budget problem

Accounting for the total oxygen budget in the ISM is a long-standing problem. In dense environments of the ISM ($n_H > 7 \text{ cm}^{-3}$), oxygen is missing from the gas phase at a level that cannot be explained simply by its depletion into dust and molecules such as CO and H₂O, and therefore additional reservoirs need to be found ([Jenkins 2009](#), [Whittet 2010](#)). In our work, we find on average that 10%–20% of oxygen is depleted into dust. Our oxygen-depletion values are consistent with those found by [Poeteet et al. \(2015\)](#), who studied the IR absorption spectra towards the diffuse-dense cloud transition region of Zeta Oph and also found that about 21% of oxygen is in dust. According to the authors, an amount of oxygen is still missing from the gas phase. A substantial fraction of interstellar oxygen could reside in other reservoirs, such as ices (H₂O) or CO.

In our study, the abundances of oxygen (both in gas and dust) along the different lines of sight fluctuate by between 20% and 40% above the Solar value ([Lodders & Palme 2009](#)). Given the typical distances to our sources of 3-8 kpc (Table 1), we get average hydrogen density of $\sim 0.1 \text{ cm}^{-3}$ for the lines of sight studied here. However, this number should be used with caution; it is merely an average over the entire spatial distribution of interstellar gas along our sight lines. It is therefore possible that in this way, we underestimate the absolute value of the hydrogen density. Nevertheless, it is interesting to compare this value to the expected partitioning between gas and solids in [Whittet \(2010\)](#), who studied the oxygen reservoirs in a wide range of interstellar environments. These latter authors found that the oxygen budget problem starts to be significant for hydrogen densities above 7 cm^{-3} . For the densities studied here, the oxygen reservoir does not appear to be a problem. Our result confirms this scenario and therefore we conclude that in this study we do not need an additional reservoir of oxygen, such as H₂O or CO.

5.5. Advantages of fitting the O and Fe together

In this work, we performed a simultaneous fit of the oxygen K and iron L edges and were able to identify the chemical composition of interstellar dust in diffuse lines of sight. In Paper I, we presented a detailed demonstration of the dust laboratory experiments in the O K-edge and fitted the oxygen K edge structure alone using XMM–Newton data. With the new dust extinction model, we are able to disentangle the dust and gas contribution in the O K-edge but we cannot distinguish among the different dust species as easily. In particular, the number of acceptable models (using the AIC criterion) in this work—where we are fitting O and Fe together—is significantly smaller than in Paper I. Therefore, by fitting two edges together, we get a better constraint on the range of possible model solutions. This allows us to identify the responsible compounds and corresponding abundances and depletion values with less uncertainty.

For the reason described above, we judge the oxygen depletion measurement for Cyg X-2 in this work to be more accurate than the value presented in our pilot study for Paper I. In Paper I, we fit the O K-edge alone and assumed that the dust chemistry is characterised by olivine only, resulting in a depletion value of 7%. In this work, for the same sight line, we find a higher value of $18 \pm 2\%$. The latter oxygen depletion value was calculated from the best-fit dust minerals, not from assuming a single dust compound. We therefore conclude that by studying the two edges simultaneously we are able to break degeneracies that might be present from the fit of a single edge, and determine the dust chemistry in these diffuse regions in the Galaxy.

In this study, we were not able to get accurate constraints on the Si and Mg abundances and depletions. For this, we will need to examine the O K, Fe L, Mg K, and Si K edges together, with a source that has the proper column density in order to give us visibility in all edges. Future X-ray observations could enable us to explore the O and Fe content of interstellar dust, together with Si and Mg, with even better accuracy. This case will be examined in a future study.

6. Conclusions

In this work, we studied the dust chemistry towards diffuse lines of sight along the Galactic plane using the soft X-ray band (< 1 keV). We simultaneously fit the absorption around the O K- and Fe L-edges using XMM–Newton and Chandra observations for five LMXBs: Cygnus X-2, Swift J1910.2-0546, XTE J1817-330, Ser X-1, and GX9+9. For the dust modelling, we use the calculated extinction models in the O K-edge presented in Psaradaki et al. (2020) and for the Fe L we use the models from Costantini et al. in prep. The dust models were computed from new laboratory data and include silicates, oxides, iron sulfides, and metallic iron. The latter was taken from the literature. Our main results can be summarised as follows.

- We were able to constrain the dust grain chemistry in the diffuse medium. Mg-rich amorphous pyroxene dust ($\text{Mg}_{0.75}\text{Fe}_{0.25}\text{SiO}_3$) represents the bulk of the dust chemistry in the diffuse environments of the ISM. In particular, we find an average of $\sim 70\%$ of this silicate towards Cygnus X-2, Swift J1910.2-0546, XTE J1817-330, and Ser X-1. Only in the line of sight towards GX 9+9 does the amorphous olivine (MgFeSiO_4) appear to be the dominant compound.
- We find an upper limit on the silicate crystallinity of 15%. This value is broadly consistent with the crystallinity observed in the IR.

- We find that on average 15% of the total dust column in our lines of sight is in the form of metallic iron.
- Iron is heavily depleted from the gas phase into dust; more than 90% of the iron is in the form of dust grains.
- 10%-20% of the neutral oxygen is depleted into dust depending on the line of sight. We also find a slight overabundance of oxygen with respect to Solar. We conclude that in the lines of sight studied here we probe a diffuse medium, and therefore there is no oxygen budget problem as has been previously found for the translucent and dense ISM regions.
- We find Solar or slightly sub-Solar abundances of iron. The latter could be attributed to self-shielding and the missing large grain population from this study ($> 0.25\mu\text{m}$). Dust extinction by large particles will be examined in a future work.
- The simultaneous fit of the O K- and Fe L-edges gave us a stronger constraint on both the dust depletion and the chemical composition of grains in the diffuse regions of the ISM.

In conclusion, our new X-ray dust-extinction cross section in the O K, and Fe L shell photoabsorption edges enabled us to understand the chemistry of interstellar dust in the diffuse lines of sight studied in this paper. Future X-ray observatories will enable us to investigate with even better accuracy the dust grain chemistry.

Acknowledgements. We thank the referee for the suggestions that helped to improve this paper. The authors would also like to thank J. de Plaa and J. Kaastra for their continuous help with SPEX. IP thanks A. Bosman for useful discussions on oxygen reservoirs. This research has been supported by the Netherlands Organisation for Scientific Research (NWO) through The Innovational Research Incentives Scheme Vidi grant 639.042.525. Portions of this work are supported by NASA's Astrophysics Data Analysis Program, grant number 80NSSC20K0883, under the ROSES program NNH18ZDA001N. The laboratory experiment related to this project has received funding from the European Union's Horizon 2020 research and innovation program under grant 823717-ESTEEM3.

References

- Akaike, H. 1974, IEEE Transactions on Automatic Control, 19, 716
- Burnham, K. P. & Anderson, D. R. 2002, Springer
- Canizares, C., Davis, J., Dewey, D., et al. 2005, Publications of the Astronomical Society of the Pacific, 117, 1144
- Cash, W. 1979, ApJ, 228, 939
- Chiar, J. E. & Tielens, A. G. G. M. 2006, ApJ, 637, 774
- Christian, D. J. & Swank, J. H. 1997, ApJS, 109, 177
- Corrales, L. R., García, J., Wilms, J., & Baganoff, F. 2016, MNRAS, 458, 1345
- Costantini, E., Pinto, C., Kaastra, J. S., et al. 2012, A&A, 539, A32
- Costantini, E., Zeegers, S. T., Rogantini, D., et al. 2019, A&A, 629, A78
- Cowley, A. P., Crampton, D., & Hutchings, J. B. 1979, ApJ, 231, 539
- de Plaa, J., Kaastra, J. S., Tamura, T., et al. 2004, A&A, 423, 49
- Demyk, K., Carrez, P., Leroux, H., et al. 2001, A&A, 368, L38
- den Herder, J. W., Brinkman, A. C., Kahn, S. M., et al. 2001, A&A, 365, L7
- Draine, B. T. 2011, Physics of the Interstellar and Intergalactic Medium
- Draine, B. T. & Hensley, B. 2013, ApJ, 765, 159
- Draine, B. T. & Hensley, B. S. 2021, The Astrophysical Journal, 909, 94
- Dwek, E. 2016, ApJ, 825, 136
- Egerton, R. 2011, Springer, Boston, MA, 3rd Edition
- Feigelson, E. D. & Babu, G. J. 2012, Modern Statistical Methods for Astronomy
- Fink, J., Müller-Heinzerling, T., Scheerer, B., et al. 1985, Phys. Rev. B, 32, 4899
- Fruscione, A., McDowell, J. C., Allen, G. E., et al. 2006, in Observatory Operations: Strategies, Processes, and Systems, ed. D. R. Silva & R. E. Doxsey, Vol. 6270, International Society for Optics and Photonics (SPIE), 586 – 597
- Galloway, D. K., Muno, M. P., Hartman, J. M., Psaltis, D., & Chakrabarty, D. 2008, ApJS, 179, 360
- Green, G. M., Schlafly, E., Zucker, C., Speagle, J. S., & Finkbeiner, D. 2019, ApJ, 887, 93
- Henning, T. 2010, ARA&A, 48, 21
- HI4PI Collaboration, Ben Bekhti, N., Flöer, L., et al. 2016, A&A, 594, A116
- Hoang, T. & Lazarian, A. 2016, ApJ, 831, 159
- Huenemoerder, D. P., Mitschang, A., Dewey, D., et al. 2011, AJ, 141, 129
- Jenkins, E. B. 2009, ApJ, 700, 1299
- Jones, A. P. & Ysard, N. 2019, A&A, 627, A38
- Kaastra, J. S. 2017, A&A, 605, A51

- Kaastra, J. S., Mewe, R., & Nieuwenhuijzen, H. 1996, in *UV and X-ray Spectroscopy of Astrophysical and Laboratory Plasmas*, 411–414
- Kaastra, J. S., Raassen, A. J. J., de Plaa, J., & Gu, L. 2018, *SPEX X-ray spectral fitting package*
- Keller, L. P. & Messenger, S. 2013, *Geochim. Cosmochim. Acta*, 107, 341
- Kemper, F., de Koter, A., Waters, L. B. F. M., Bouwman, J., & Tielens, A. G. G. M. 2002, *A&A*, 384, 585
- Kemper, F., Vriend, W. J., & Tielens, A. G. G. M. 2004, *ApJ*, 609, 826
- Kortright, J. B. & Kim, S.-K. 2000, *Phys. Rev. B*, 62, 12216
- Lee, J. C. 2010, *Space Sci. Rev.*, 157, 93
- Lee, J. C. & Ravel, B. 2005, *ApJ*, 622, 970
- Lee, J. C., Xiang, J., Ravel, B., Kortright, J., & Flanagan, K. 2009, *ApJ*, 702, 970
- Lodders, K. & Palme, H. 2009, *Meteoritics and Planetary Science Supplement*, 72, 5154
- Mathis, J. S., Rimpl, W., & Nordsieck, K. H. 1977, *ApJ*, 217, 425
- McClintock, J. E., Remillard, R. A., Petro, L. D., Hammerschlag-Hensberge, G., & Proffitt, C. R. 1984, *ApJ*, 283, 794
- Mie, G. 1908, *Annalen der Physik*, 330, 377
- Min, M., Waters, L. B. F. M., de Koter, A., et al. 2007, *A&A*, 462, 667
- Molster, F. J., Waters, L. B. F. M., & Tielens, A. G. G. M. 2002, *A&A*, 382, 222
- Newville, M. 2004, *Consortium for Advanced Radiation Sources, University of Chicago (USA)*[<http://xafs.org>], 78
- Paelers, F., Brinkman, A. C., van der Meer, R. L. J., et al. 2001, *ApJ*, 546, 338
- Pinto, C., Kaastra, J. S., Costantini, E., & de Vries, C. 2013, *A&A*, 551, A25
- Poteet, C. A., Whittet, D. C. B., & Draine, B. T. 2015, *ApJ*, 801, 110
- Psaradaki, I., Costantini, E., Mehdipour, M., et al. 2020, *arXiv e-prints*, arXiv:2009.06244
- Reis, R. C., Reynolds, M. T., Miller, J. M., et al. 2013, *ApJ*, 778, 155
- Rogantini, D., Costantini, E., Zeegers, S. T., et al. 2018, *A&A*, 609, A22
- Rogantini, D., Costantini, E., Zeegers, S. T., et al. 2019, *A&A*, 630, A143
- Rogantini, D., Costantini, E., Zeegers, S. T., et al. 2020, *A&A*, 641, A149
- Sala, G. & Greiner, J. 2006, *The Astronomer's Telegram*, 791, 1
- Schalen, C. 1965, *PASP*, 77, 409
- Schattenburg, M. L. & Canizares, C. R. 1986, *ApJ*, 301, 759
- Schlegel, D. J., Finkbeiner, D. P., & Davis, M. 1998, *ApJ*, 500, 525
- Shahbaz, T., Smale, A. P., Naylor, T., et al. 1996, *MNRAS*, 282, 1437
- Smale, A. P. 1998, *ApJ*, 498, L141
- Tamanai, A., Pucci, A., Dohmen, R., & Gail, H.-P. 2017, *The Astrophysical Journal*, 845, 6
- Thorstensen, J. R., Charles, P. A., & Bowyer, S. 1980, *ApJ*, 238, 964
- Torres, M. A. P., Steeghs, D., McClintock, J., et al. 2006, *The Astronomer's Telegram*, 749, 1
- Ueda, Y., Mitsuda, K., Murakami, H., & Matsushita, K. 2005, *ApJ*, 620, 274
- van de Hulst, H. C. 1957, *Light Scattering by Small Particles*
- Vilhu, O., Paizis, A., Hannikainen, D., Schultz, J., & Beckmann, V. 2007, in *ESA Special Publication, Vol. 622, The Obscured Universe. Proceedings of the VI INTEGRAL Workshop*, 421
- Westphal, A. J., Butterworth, A. L., Tomsick, J. A., & Gainsforth, Z. 2019, *ApJ*, 872, 66
- Whittet, D. C. B. 2010, *ApJ*, 710, 1009
- Wilms, J., Allen, A., & McCray, R. 2000, *ApJ*, 542, 914
- Zeegers, S. T., Costantini, E., de Vries, C. P., et al. 2017, *A&A*, 599, A117
- Zeegers, S. T., Costantini, E., Rogantini, D., et al. 2019, *A&A*, 627, A16
- Zhukovska, S., Henning, T., & Dobbs, C. 2018, *ApJ*, 857, 94

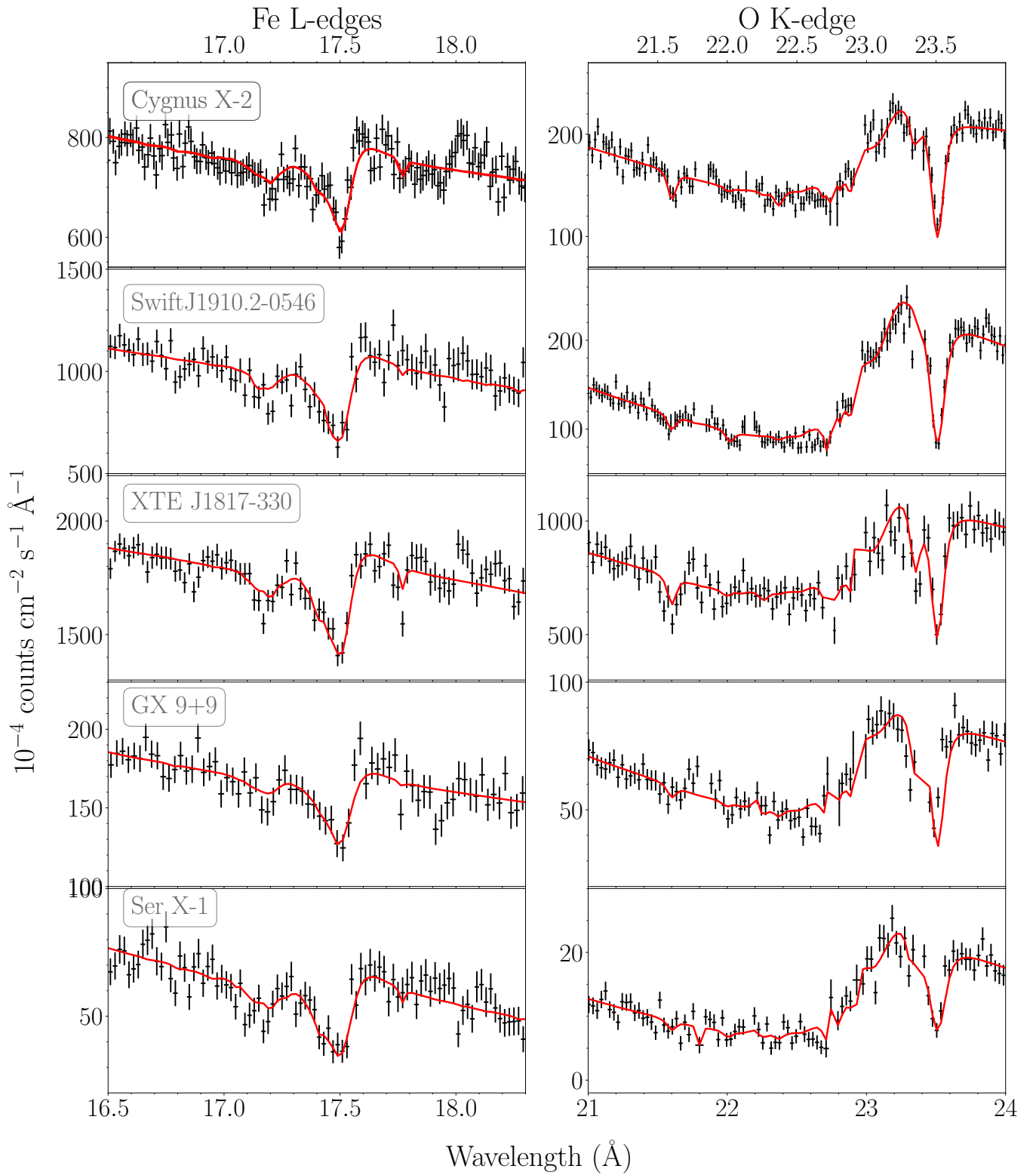


Fig. 3. Best fit in the O K and Fe L-edges. XMM-Newton data were used to fit the O K-edge spectral region, while for the Fe L-edges we use spectroscopic data from Chandra. The spectral fitting has been done by taking into account both gas (neutral+ionised) and dust absorption.

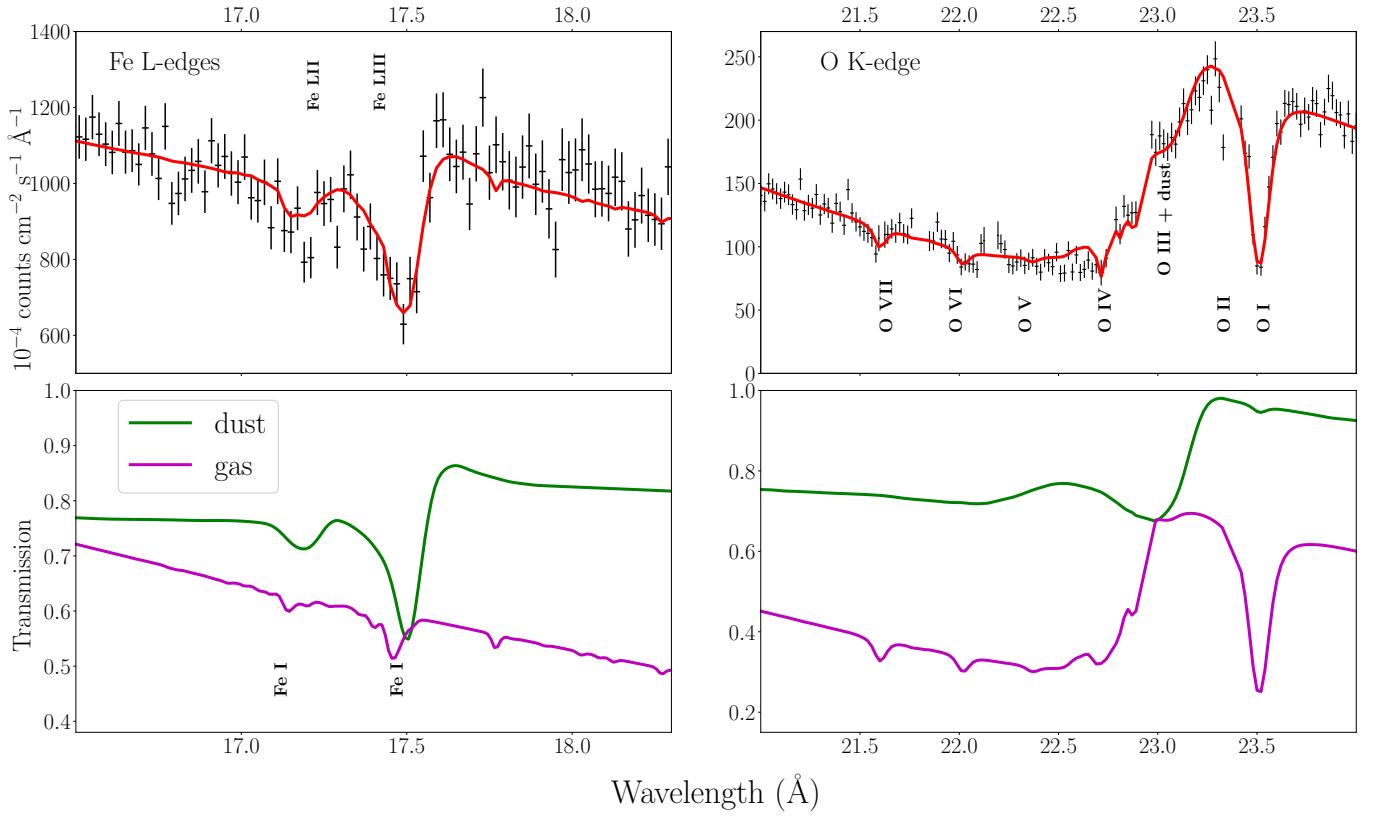


Fig. 4. Best fit in the O K and Fe L-edges for SWIFT J1910.2–0546 and the relative transmission for the gas and dust components. The transmission of the gas has been multiplied by factors of 2.5 and 4.5 for iron and oxygen, respectively, for display purposes.

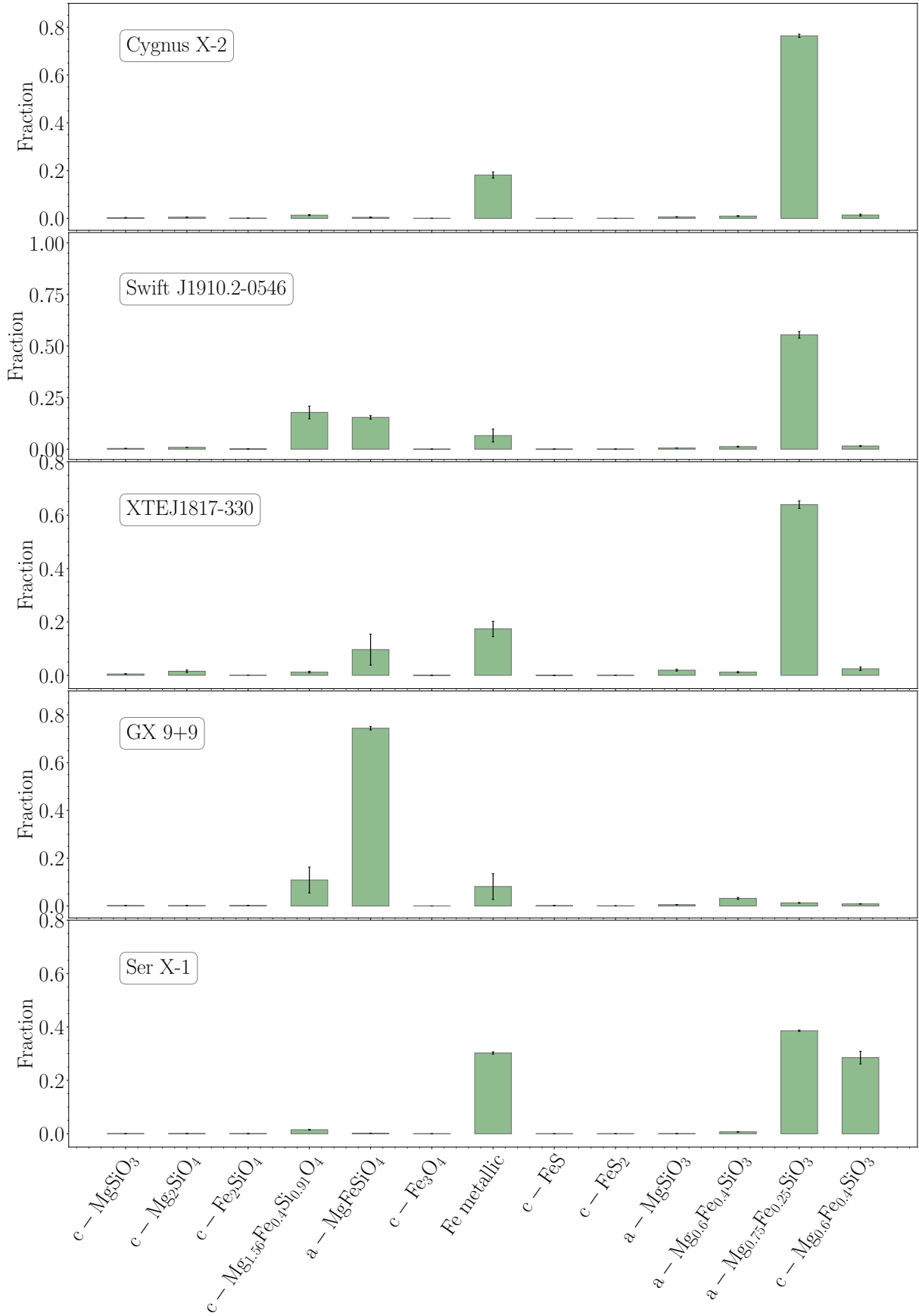


Fig. 5. Relative fraction of column density for each dust compound. The fraction was calculated considering models with $\Delta\text{AIC} < 4$. The symbol *a* refers to amorphous compounds and *c* to crystalline. The errors on the bar charts are an indication of the minimum and maximum percentage of each compound within the $\Delta\text{AIC} < 4$ selected models. For the least significant compounds, the reported values are an indication of an upper limit.